Supporting Information

Green and Tough Eutectogel from Demethylated Lignin: Bridging Renewable Biomass and Harsh-Environment Sensing

Jinwen Hu,‡[a] Yueying Zhao,‡[a] Tingjun Song,[a] Bo Pang,[b] Tingting Wang,[a] Siying Zhou,[a] Jian Du,[a,c] Yanna Lv,[a] Yehan Tao,[a] Jie Lu,[a] Chenglong Fu[a] and Haisong Wang*[a]

[a] College of Light Industry and Chemical Engineering, Dalian Polytechnic University, Dalian 116034, China. E-mail: wanghs@dlpu.edu.cn.

[b] Department of Food Science and Technology, National University of Singapore, Singapore 117542, Singapore

[c] Department of Materials Science and Engineering, Pohang University of Science and Technology, Pohang 37673, Republic of Korea

1. Experimental section

1.1. Characterizations

For 2D-HSQC ^{13}C NMR characterization, precisely 40 mg of the lignin sample was completely dissolved in 500 μL of deuterated dimethyl sulfoxide (DMSO-d6) and subsequently transferred to a standard 5 mm NMR tube. Parallel ^{1}H NMR measurements were conducted by dissolving 25 mg of lignin with 10 μL of pentafluorobenzaldehyde (as internal standard) in 0.55 mL of DMSO-d6, followed by transfer to an NMR tube. All NMR spectra were acquired on a Bruker AVIII 400 MHz spectrometer. For optimal signal-to-noise ratio, each spectrum was collected with 32 scans. Quantitative analysis of methoxy group content was performed using the following calculation method:

$$C_{OCH_3}(mmol/g) = \frac{m_1 \times s_1}{3 \times S_2 \times M_1 \times m_2} \quad \textbf{(Equation S1)}$$

C_{OCH3} is the content of methoxy. M_1 and m_1 are the molar mass and mass of pentafluorobenzaldehyde. m_2 is the mass of lignin. S_1 is the integration of resonance peak of the methoxy group, and S_2 is the integration of resonance peak of pentafluorobenzaldehyde (=1).

GPC analysis was performed using an Agilent 1200 GPC equipped with a PL-gel 10mm mixed-B column (7.5 mm internal diameter). Prior to analytical characterization, lignin samples underwent acetylation following an optimized derivatization procedure. Exactly 20.0 mg of lignin sample was first dissolved in 0.5 mL anhydrous pyridine within a nitrogen-purged glass reactor. Subsequently, 0.5 mL acetic anhydride was added via precision microsyringe under continuous magnetic stirring (300 rpm). The reaction system was maintained at 80°C for 4h to ensure complete acetylation. After cooling to room temperature (25°C), the reaction was quenched by dropwise addition into 100 mL of ice-cold deionized water. The precipitate was collected through high-speed centrifugation and subjected to three successive wash cycles with 30 mL ultrapure water per cycle. The purified product was finally lyophilized for 48h to obtain acetylated lignin. For GPC analysis, the acetylated lignin was dissolved in tetrahydrofuran (THF) at a concentration of 2 mg/mL. The solution was filtered through a 0.22 μm PTFE membrane filter to remove particulate matter. Chromatographic separation was performed at a constant flow rate of 1.0 mL/min with the column temperature maintained at 30°C.

The cross-sectional microstructures of samples were investigated on a scanning electron microscope (SEM, JSM-7800F, Japan) at an accelerating voltage of 3 kV.

The chemical structure was detected with the Fourier transform infrared spectroscopy (FTIR) spectrometer (PerkinElmer, Limited by Share Ltd., USA) from 400 cm^{-1} to 4000 cm^{-1} with a resolution of 1 cm^{-1} in the transmission mode.

Transmittance and absorbance of samples were collected using a UH5300 UV-vis spectrophotometer with a scanning rate of 200 nm/min, testing range 200-800 nm.

Hydrophobic micelles of gel prepolymers were observed by biological microscopy (DMC 2900, LEICA).

1.2. Aqueous phase potentiometric titration

30 mg of the raw Kraft lignin or DL was dispersed in 5 mL of KOH solution (pH ≈ 12) for alkalinization. Subsequently, 50 mg of p-hydroxybenzoic acid (internal standard) was added to the suspension. Then, 25 ml of deionized water was added and sonicated for 30 minutes to ensure complete dissolution of both lignin and internal standard. A blank control was prepared following the identical protocol but omitting the lignin. 0.1 M hydrochloric acid solution was served as the titrant.

The hydroxyl content was calculated as follows:

$$C_{Ar-OH}(mmol/g) = \frac{\left[\left(V_2^{'} - V_1^{'}\right) - \left(V_2 - V_1\right)\right]C_{HCl}}{m} \quad \textbf{(Equation S2)}$$

where $C_{(Ar\text{-}OH)}$ was the content of Ar-OH. C_{HCl} was the concentration of standard hydrochloric acid solution. m was the absolute dry mass of the sample. V_1 and V_2 were the hydrochloric acid volume corresponding to the first 2 peaks of the differential titration curve of the blank sample, respectively. V_1' and V_2' were the hydrochloric acid volume corresponding to the first 2 peaks of the differential titration curve of the lignin sample, respectively.

1.3. Performance characterization of eutectogel

Mechanical properties: a universal materials testing machine (Instron 5965, USA) was used to measure the mechanical properties of eutectogel at room temperature. The eutectogel with a size of 45 mm long x 12 mm wide x 1.7 mm thickness was used for uniaxial tensile tests. The ends of the sample were clamped and stretched at a constant rate of 100 mm min^{-1}. Three specimens were tested, and the average value was calculated to determine each property. Tensile cycling tests were carried

out under the same conditions to assess the fatigue resistance of the samples. The mechanical properties before and after self-repairing were compared to evaluate the self-repairing efficiency of the material.

The tensile stress (T) was calculated as

$$T = F/S \quad \textbf{(Equation S3)}$$

where F was the tensile load and S was the cross-sectional area.

The toughness of the eutectogel was estimated according to the integral area of the stress-strain curve from 0% strain to the fracture strain (ζ_β) by following equation:

$$E = \int_0^{\zeta_\beta} \sigma(\zeta) d\zeta \quad \textbf{(Equation S4)}$$

Compression tests: the compressive stress (C) was calculated as follow:

$$C = f/s \quad \textbf{(Equation S5)}$$

where f was the compressive load and s was the original area of the sample. The crosshead speed during compression was maintained at 10 mm min^{-1}. Compressive modulus of the eutectogel was calculated from the slope of the stress-strain curve within the 0-50% strain range.

Adhesion property: The adhesive property of the samples was characterized by peel experiment. The eutectogel sample with a size of 20 mm × 20 mm × 1.7 mm was sandwiched between two pieces of substrates and stretched with vertically opposite forces for the tensile test. The stretching rate of the tests was set as 10 mm min^{-1}.

Swelling Behavior Analysis: The pH-responsive swelling characteristics were investigated through gravimetric analysis under controlled conditions. Cylindrical gel specimens were accurately weighed and individually immersed in 25 mL of phosphate-buffered solutions spanning pH 1-11 at 25°C. At 24h intervals, samples were carefully retrieved, surface-adherent liquid was absorbed by lint free cloths, and their mass was immediately measured with an analytical balance. The swelling ratio (SR) was calculated as:

$$SR\ (\%) = \frac{(Wi - W0)}{W0} \times 100\% \quad \textbf{(Equation S6)}$$

where W_0 and W_i represented the initial dry mass and the swollen mass at time t, respectively. Buffer solutions were refreshed daily to maintain ionic strength and pH stability. Measurements were

performed at regular intervals until equilibrium swelling was attained.

Water contact angle (WCA) was tested under ambient (25 ℃ and 50 % RH) by automatic contact angle absorption analyzer (DAT1122, Sweden).

Differential scanning calorimeter (DSC)：The eutectogel sample (5-10 mg) in an aluminum pan was analyzed using DSC (TA Q2000). The sample was cooled from 25 ℃ to - 80 ℃ at a rate of 10 ℃ min^{-1}, held at -80 ℃ for 2 min, and then heated to 80 ℃. Finally, the sample was cooled from 80 ℃ to 25 ℃. The heat flux data during warming and cooling processes were monitored under automated temperature program control.

Conductivity property of gel: the electrical property of the eutectogel was determined using an electrochemical workstation (Chi660E, CH Instruments Ins, China). The columnar eutectogel resistance was measured using electrochemical impendence spectroscopy (EIS), and the ionic conductivity (σ) was calculated using the following equation:

$$\sigma = R/LS \quad \textbf{(Equation S7)}$$

where L, R, and S represented the distance between the two adjoining electrodes, resistance, and cross-sectional area of the eutectogel, respectively.

The real-time resistance (R) detection was conducted using a Keithley DMM7510 $7^1/_2$-digit multimeter (Tektronix, USA).

The antimicrobial efficacy was evaluated using a modified oscillation method. Cryopreserved Gram-negative Escherichia coli (*E. coil*) and Gram-positive Staphylococcus aureus (*S. aureus*) were revived on lysogeny broth (LB) agar at 37 °C for 24h. Subsequently, 0.2 mL colonies were inoculated into 5 mL sterile tryptic soy broth and cultured at 200 rpm. Sterilized eutectogel specimens (0.1 g) were then immersed in a mixed solution consisting of 1 mL as-prepared bacterial suspension and 4 mL sterile 0.9% NaCl solution. The mixtures were subjected to continuous oscillation at150 rpm and 37.0 °C for 24h using an air shock shaker. Serial decimal dilutions (10^{-1} to 10^{-4}) were prepared in sterile 0.9% NaCl solution. Aliquots (100 μL) from appropriate dilutions were spread-plated on LB agar and incubated at 37 °C for 24h. The antibacterial activity (R) was calculated as follow:

$$Antibacterial\ Rate\ (\%) = \frac{(Ncontrol - NSample)}{Ncontrol} \times 100\% \quad \textbf{(Equation S8)}$$

where $N_{control}$ and N_{sample} represented the count of visible colonies in the control group and tested

group, respectively.

2. Figures

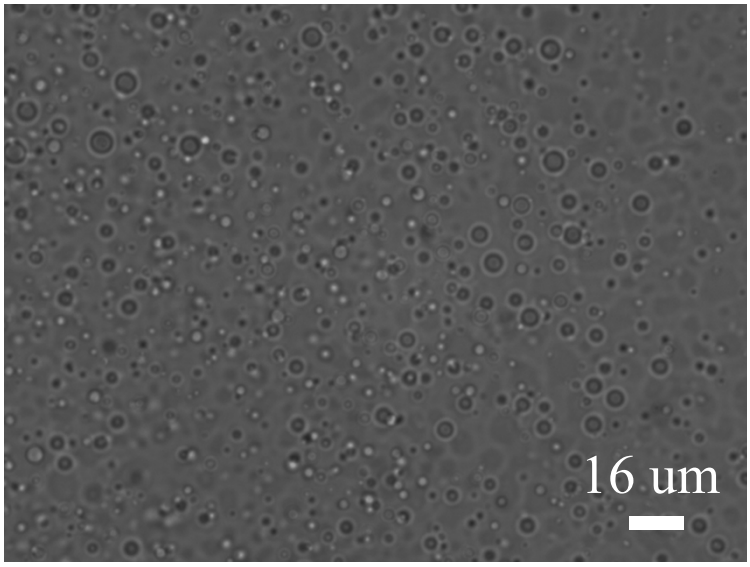

Fig. S1 Hydrophobic micelles of eutectogel (DA_5-PDES-DL_2) prepolymers.

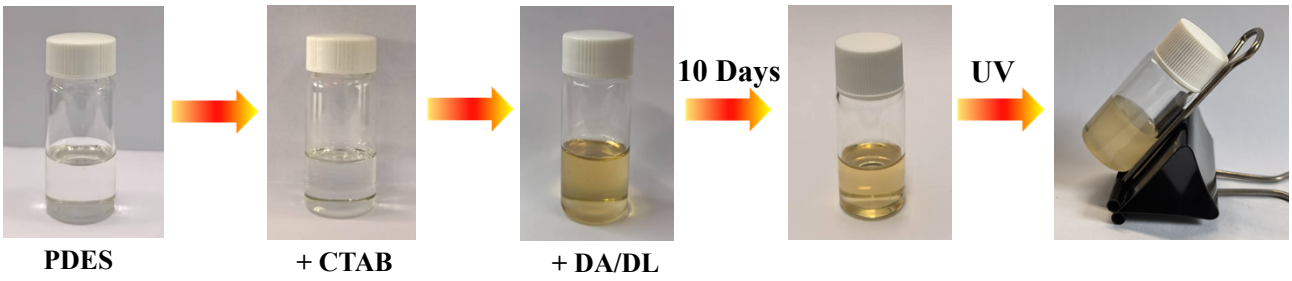

Fig. S2 Phase evolution of the precursor solution during eutectogel synthesis. The homogeneous transparent precursor solution prepared by thoroughly mixing these eutectogel precursors remained undisturbed under ambient conditions for 10 days, maintaining its uniform transparency throughout the observation period. Subsequent UV irradiation successfully transformed the stable mixture into a homogeneous eutectogel, thereby confirming both the excellent stability of the precursor solution and the successful coexistence of multiple phases in the system.

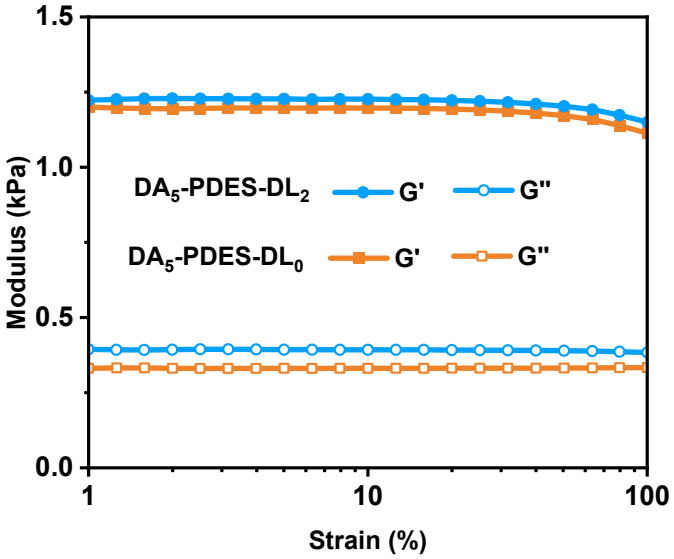

Fig. S3 The rheological strain sweep curves of DA_5-PDES-DL_2 and DA_5-PDES-DL_0 euthectogels.

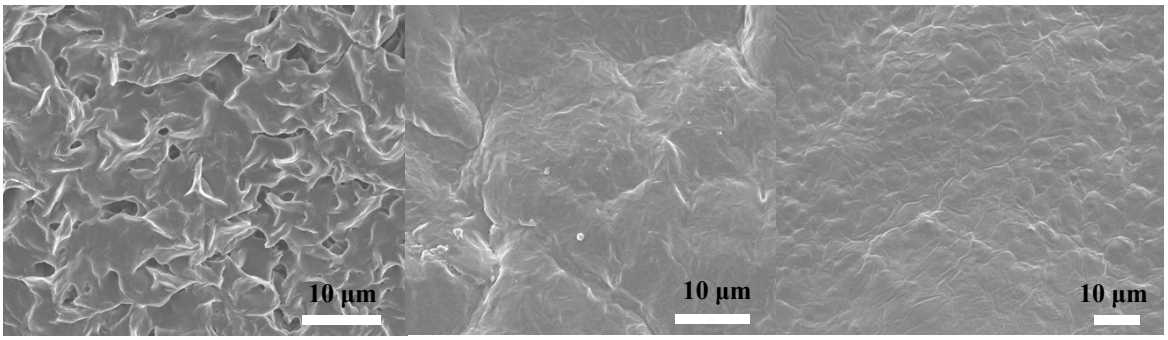

DA_0-PDES-DL_0 **DA_5-PDES-DL_0** **DA_5-PDES-DL_2**

Fig. S4 Micromorphology evolution of eutectogel with the addition of DA and DL. This structural densification will effectively restrict water infiltration within the eutectogel matrix.

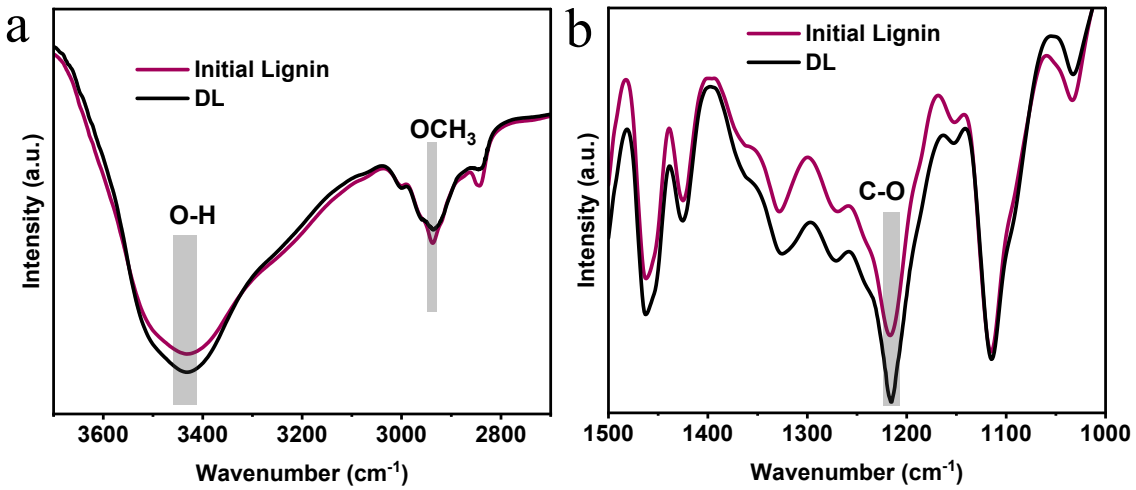

Fig. S5 Infrared spectra with magnified regions.

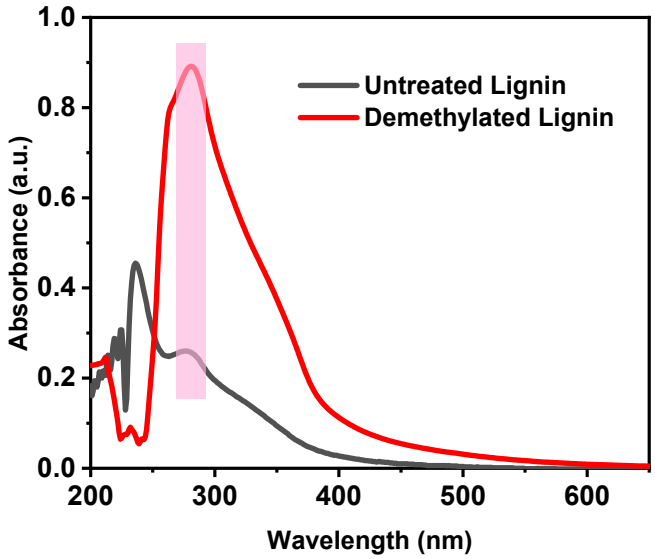

Fig. S6 UV-vis spectra of untreated lignin and demethylated lignin.

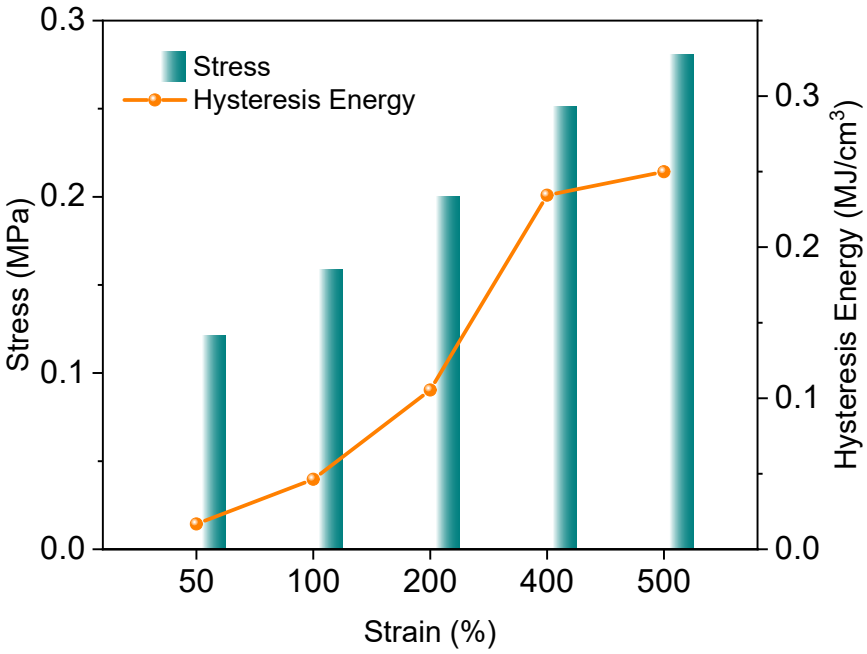

Fig. S7 Hysteresis energy and tensile stress of DA_5-PDES-DL_2 under different strain cycles.

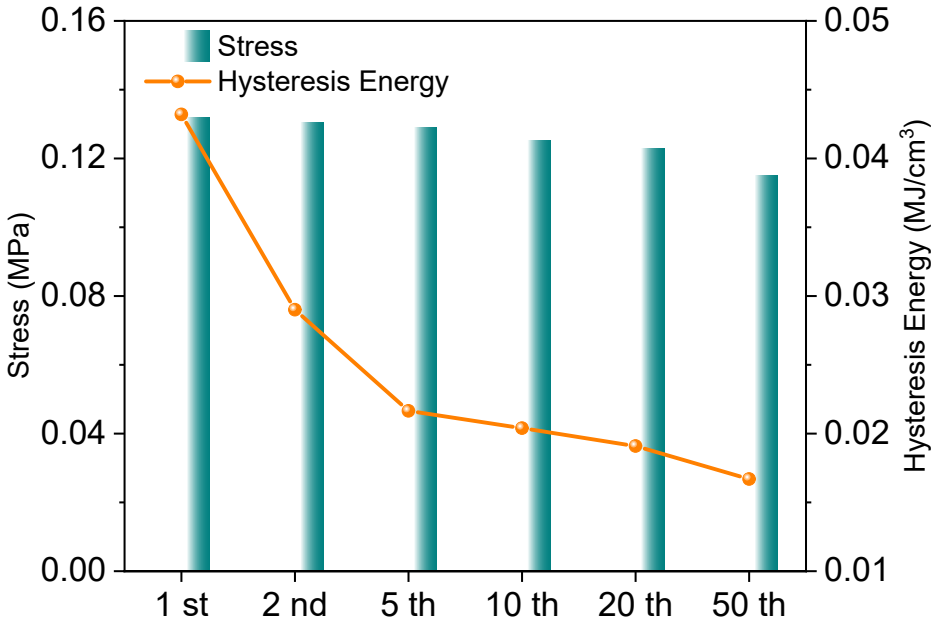

Fig. S8 Hysteresis energy of DA_5-PDES-DL_2 cycling at 100% strain.

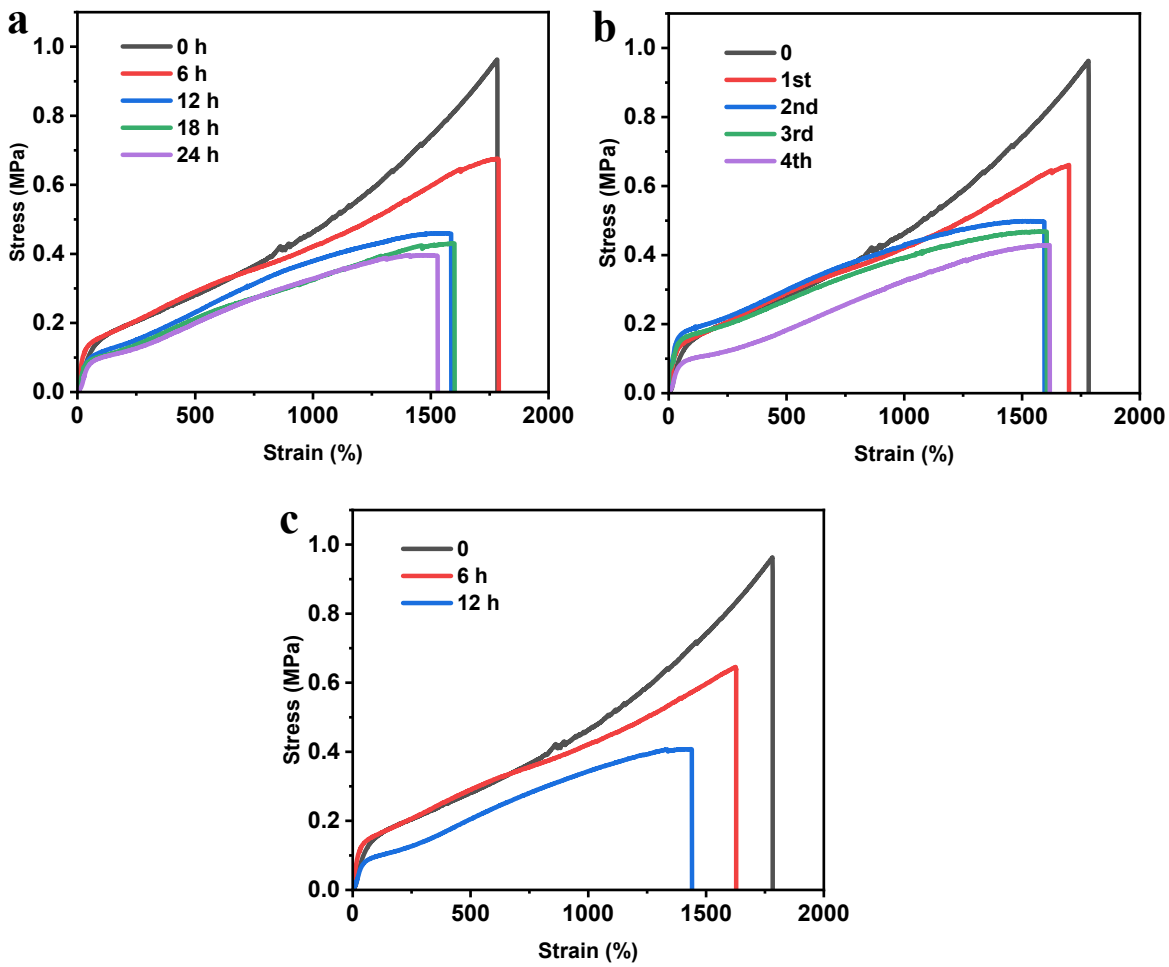

Fig. S9 Aging and stability testing under various conditions: (a) Normal temperature environment; (b) freeze-thaw cycles; (c) water immersion. The freshly prepared eutectogel was put into air for aging, and the stretchability was tested every 6 h. In the first 6 h, the stress slightly decreased. Then the stress-strain significantly decreased, and after 12 h, the mechanical properties tended to stabilize. After 24 h, it could still maintain ~86% of the initial fracture strain and ~42% of the initial fracture stress. Then, the freshly prepared eutectogel was subjected to freeze-thaw cycles by freezing at -20 ℃ for 18 h followed by thawing at room temperature, with its tensile properties being tested after each complete cycle. During the first two freeze-thaw cycles, its stretchability dropped significantly. Beyond two cycles, however, its mechanical properties stabilized, maintaining 52.1% of the initial fracture stress and 89.5% of the initial fracture strain. Finally, when the freshly prepared eutectogel was immersed in water for 12 h, its mechanical property decreased significantly. Considering the anti-swelling property of eutectogel, the above result showed that even if a small amount of water was immersed, the mechanical properties of eutectogel will be significantly affected.

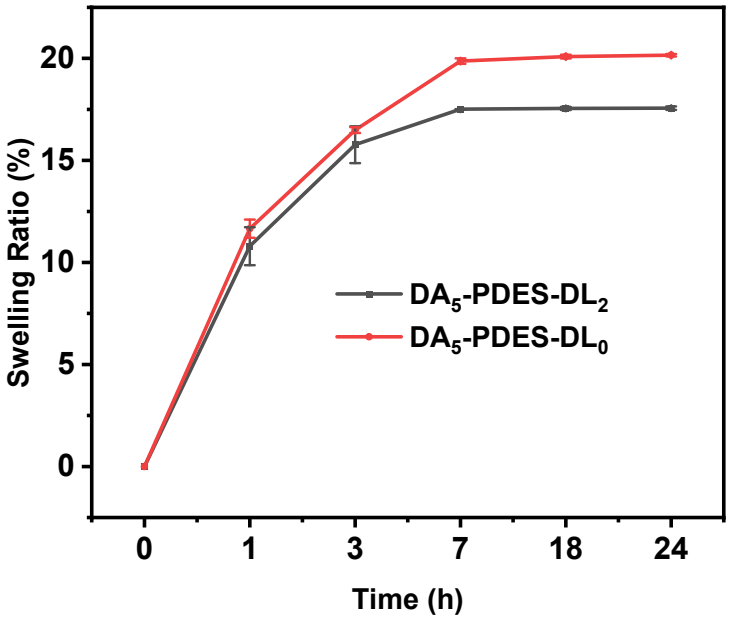

Fig. S10 DA_5-PDES-DL_2 and DA_5-PDES-DL_0 swelling curves.

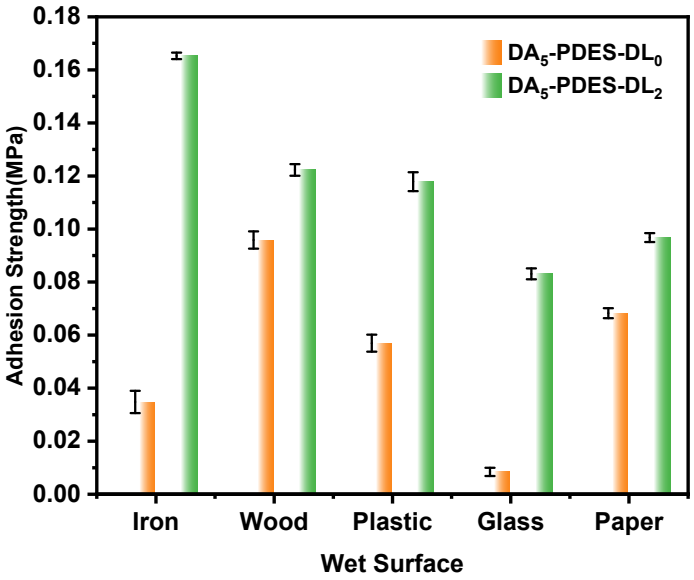

Fig. S11 The wet adhesion strength of DA_5-PDES-DL_2 and DA_5-PDES-DL_0 to different substrates (165 ± 1.2 kPa to wet metal).

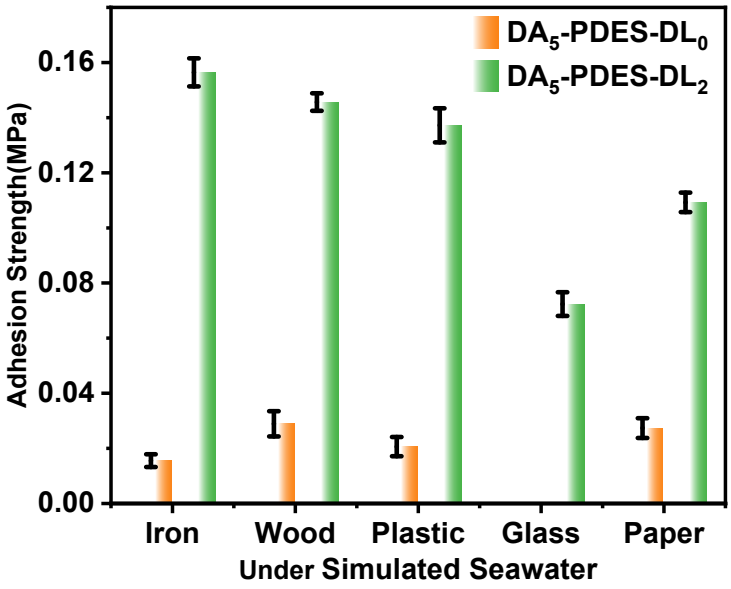

Fig. S12 Adhesion of DA_5-PDES-DL_2 and DA_5-PDES-DL_0 to different substrates in simulated seawater environment.

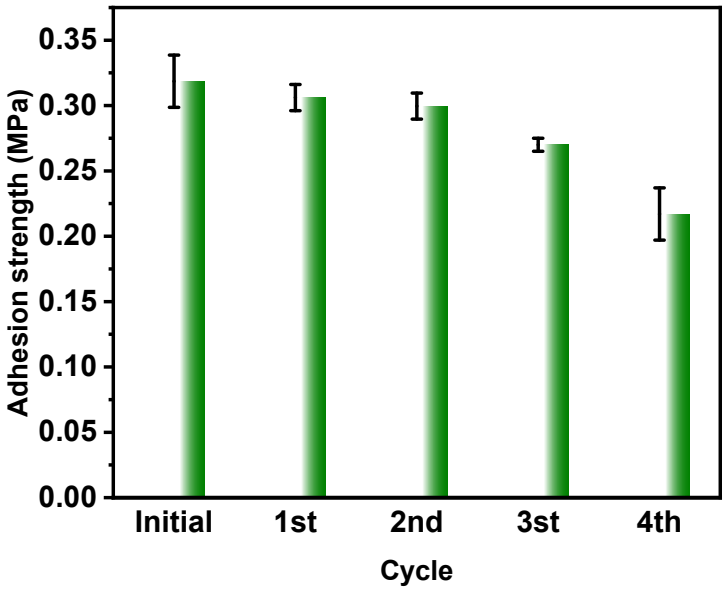

Fig. S13 Adhesion of eutectogel to plastic during the freeze-thaw cycles. The freshly prepared eutectogel was subjected to freeze-thaw cycles by freezing at -20 ℃ for 18 h followed by thawing at room temperature. The change of interfacial adhesion after each freeze-thaw cycle was studied by taking the adhesion of eutectogel to plastic as an example. It can be clearly observed the eutectogel maintained strong adhesion to plastic after initial freeze-thaw cycle. However, a significant reduction in adhesion strength occurred after the fourth cycle, likely due to a certain degree of chemical structure damage of the eutectogel surface caused by prolonged freezing.

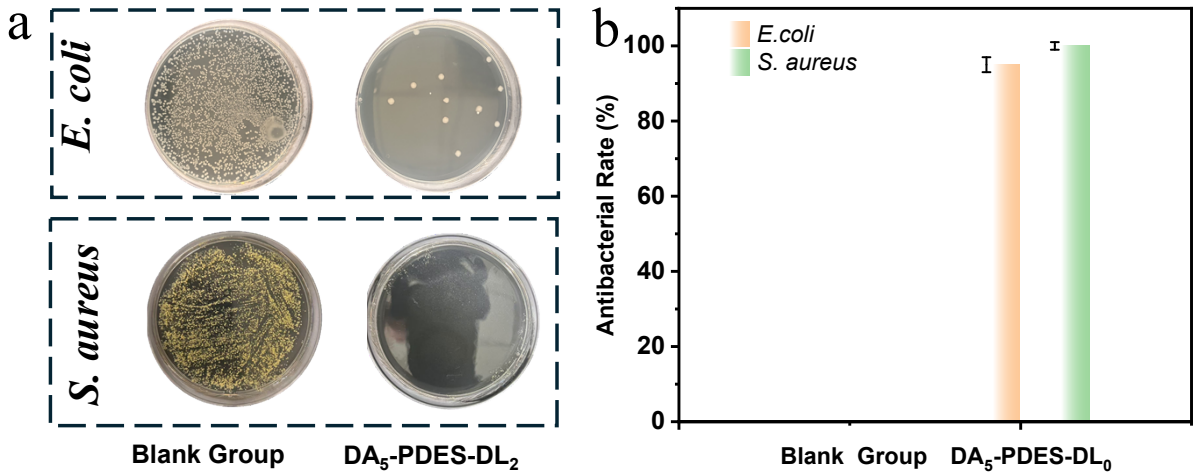

Fig. S14 Antibacterial plate and antibacterial efficiency of DA_5-PDES-DL_2.

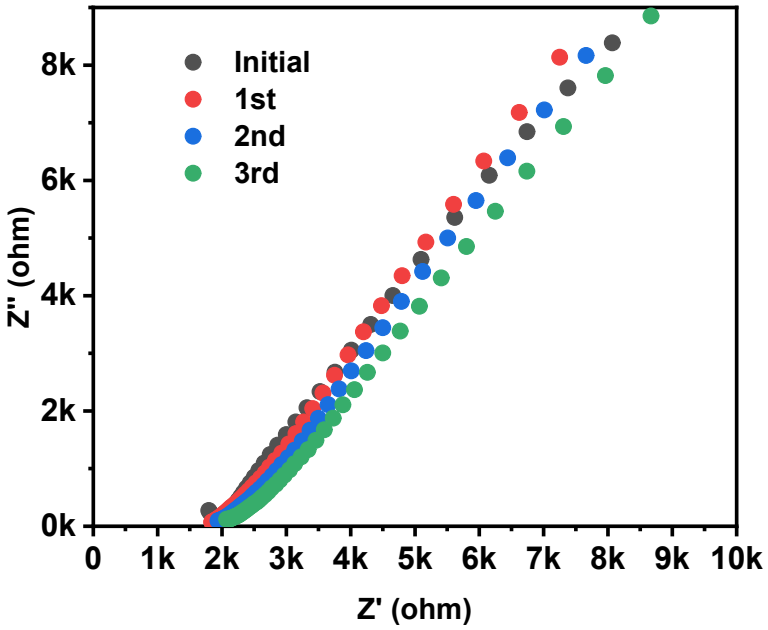

Fig. S15 Impedance curve of eutectogel during the freeze-thaw cycles. Regarding the electrical conductivity, the change in conductivity after each freeze-thaw cycle was calculated. The eutectogel retained considerable conductivity (0.46 ± 0.03 $S \cdot m^{-1}$) even after extended freeze-thaw cycling.

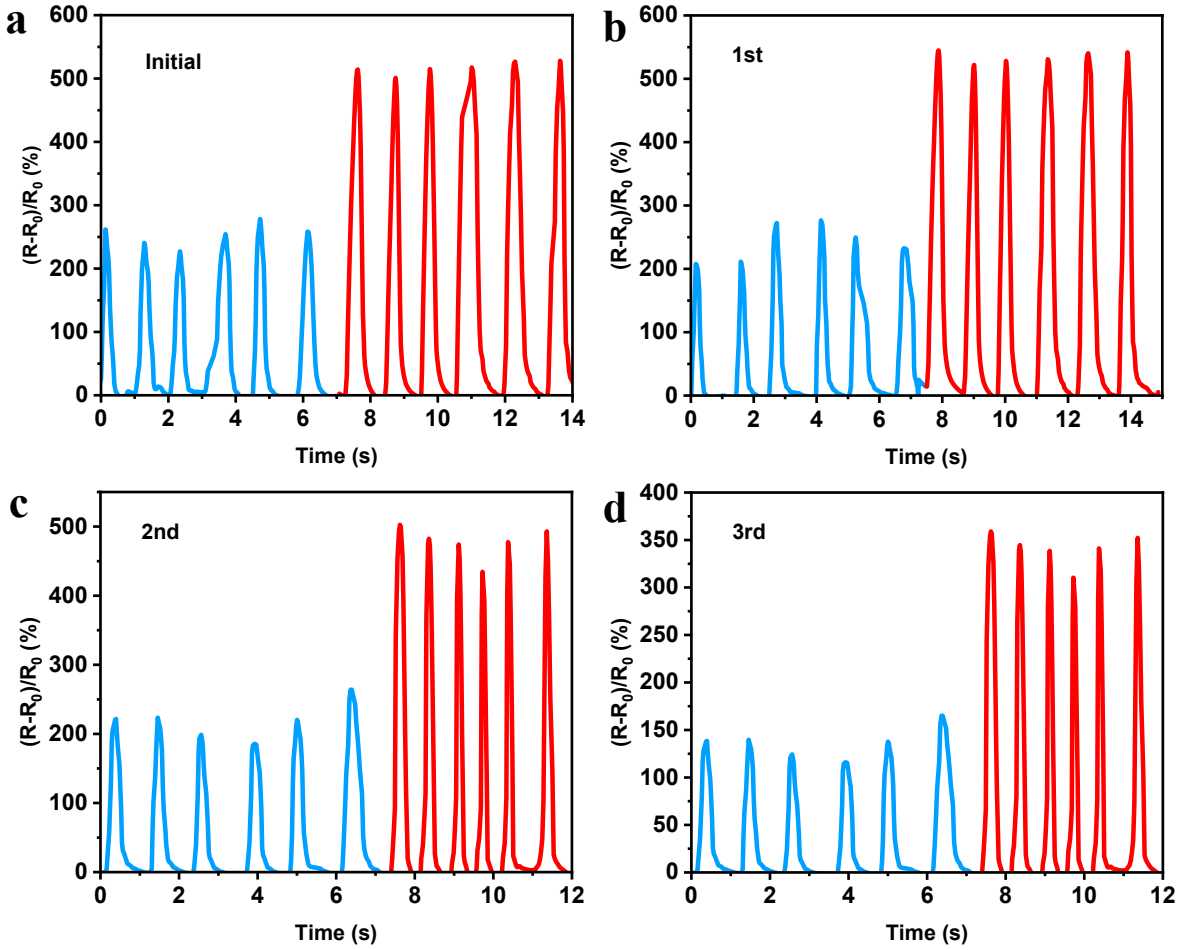

Fig. S16 Relative resistance changes of eutectogel under different strains during the freeze-thaw cycles.

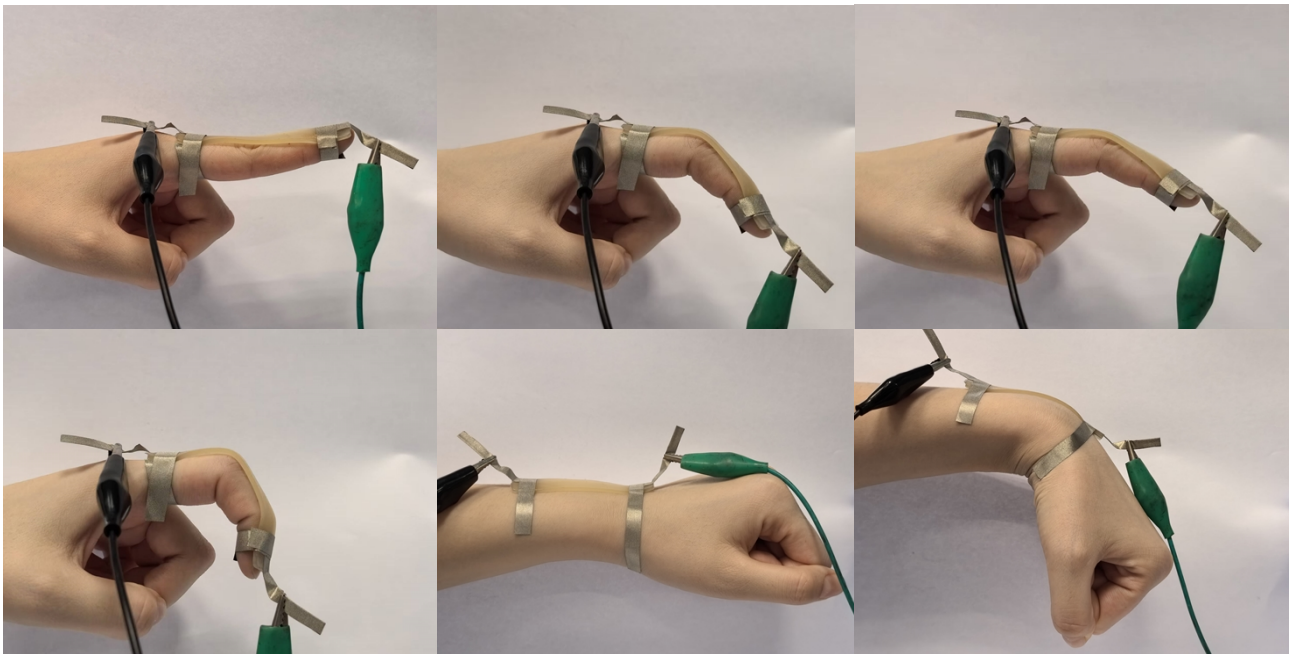

Fig. S17 The setup and application of eutectogel sensor adhered to fingers and wrists at different bending angles.

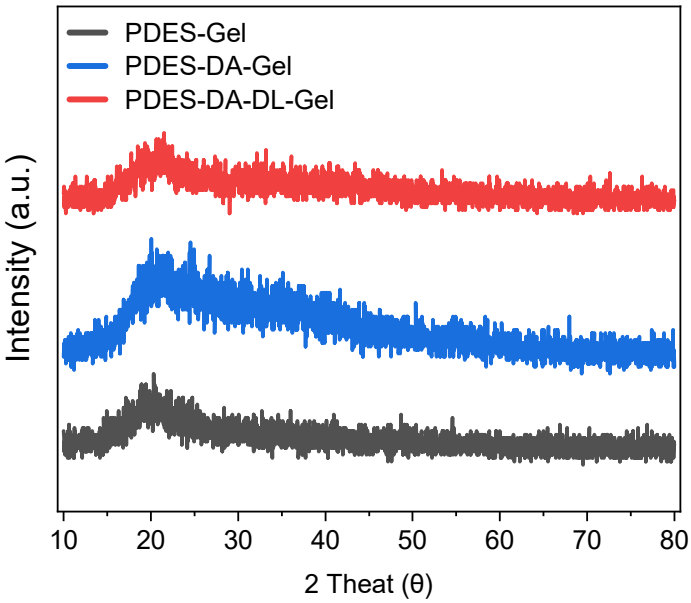

Fig. S18 The XRD spectra of different gel.

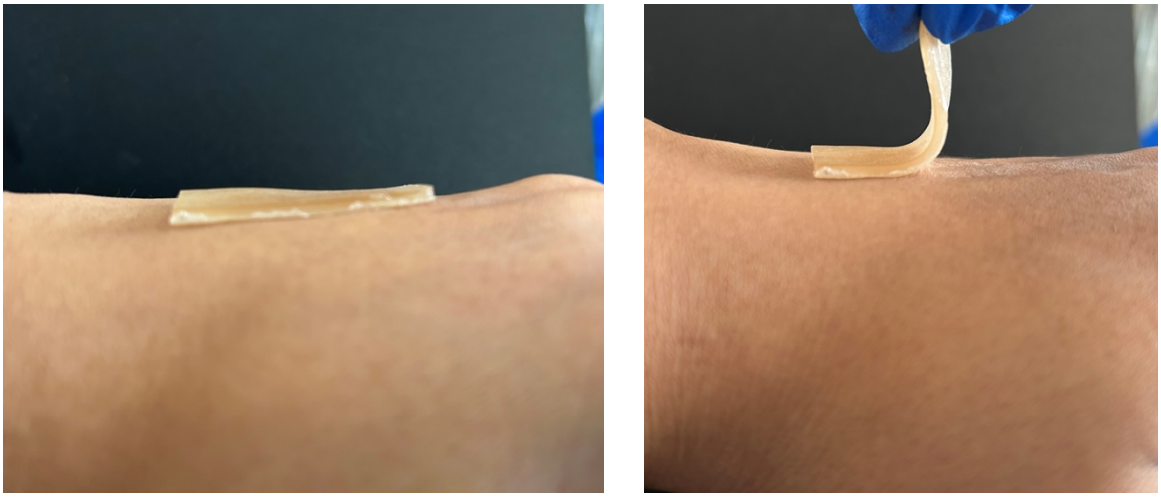

Fig. S19 Strong adhesion of DA_5-PDES-DL_2 Eutectogel on human skin.

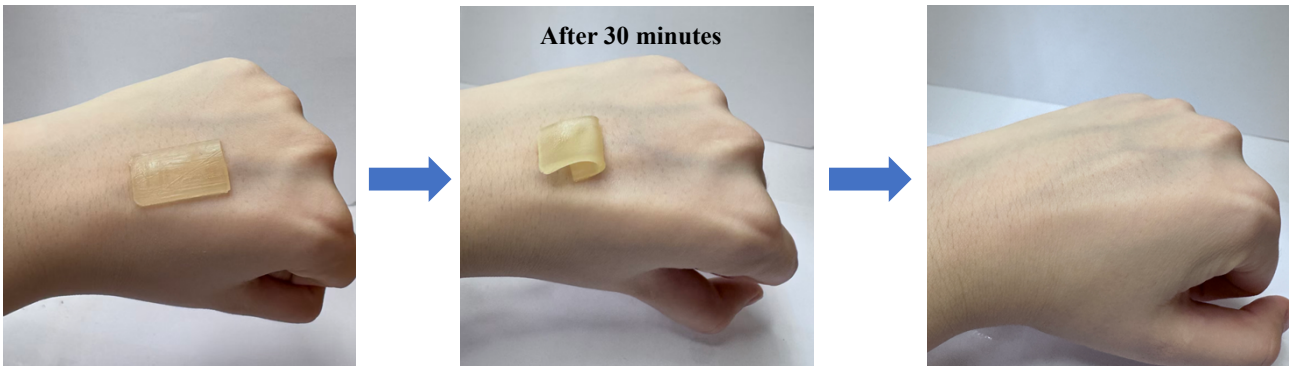

Fig. S20 The eutectogel adhered to the back of a hand for 30 minutes without skin irritation or sensitization.

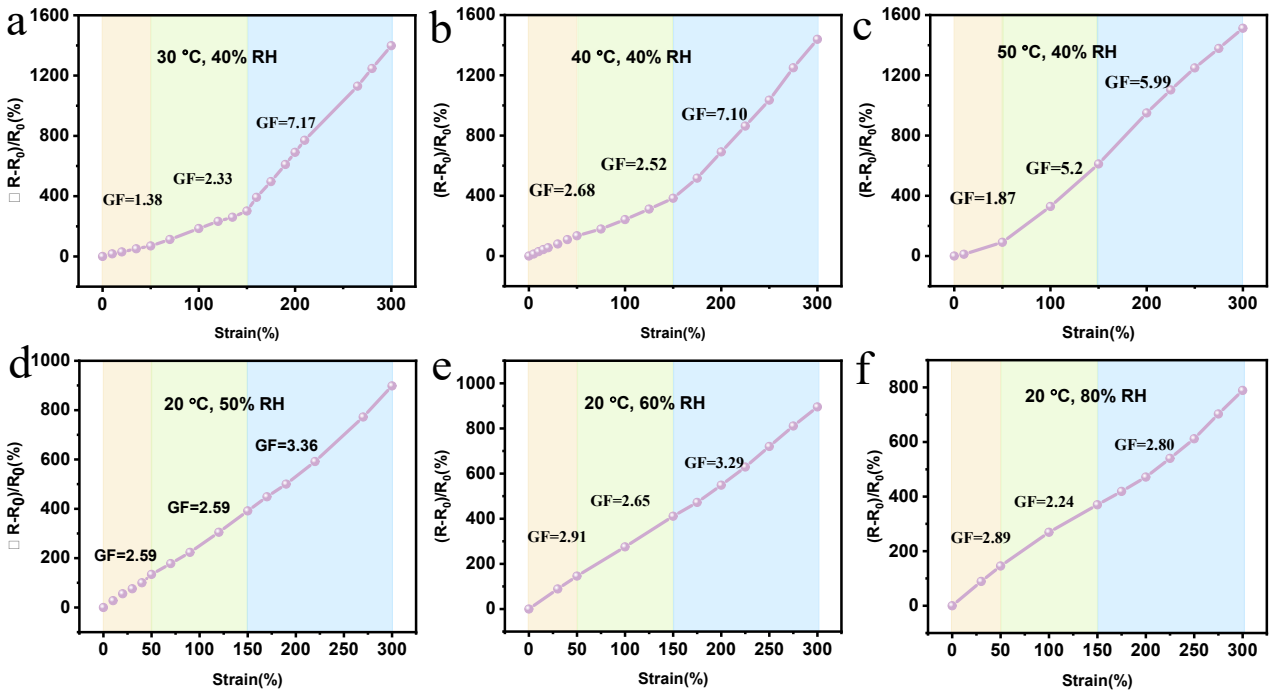

Fig. S21 The influence of temperature, relative humidity (RH), and strain on GF. Under identical temperature and RH conditions, the GF increased with increasing strain. At a constant RH of 40%, as temperature rose, GF initially increased and then decreased at low strain levels, while it continuously increased at moderate strain and continuously decreased at high strain levels (Fig. S21a-c). At a constant temperature of 20 °C, as the RH increased, GF first increased and then decreased under low and medium strain conditions, and continued to decrease under high strain conditions (Fig. S21d-f).

Fig. S22 Hemolysis ratio of DA_5-PDES-DL_2 eutectogel and the photographs. Negative control is erythrocyte suspension incubated in normal saline while positive control is erythrocyte suspension incubated in deionized water at 37 °C. Quantitative analysis shown that the HR of the target sample is (4.6 ± 0.2)%.

Table S1. The precursor composition of eutectogels

Sample	DA [g]	PDES [g]	CTAB [g]	I2959 [mg]	water [g]	DL [mg]
DA_1-PDES-DL_0	0.1	8.5	1	25	0.5	0
DA_3-PDES-DL_0	0.3	8.5	1	25	0.5	0
DA_5-PDES-DL_0	0.5	8.5	1	25	0.5	0
DA_7-PDES-DL_0	0.7	8.5	1	25	0.5	0
DA_5-PDES-DL_1	0.5	8.5	1	25	0.5	1
DA_5-PDES-DL_2	0.5	8.5	1	25	0.5	2
DA_5-PDES-DL_4	0.5	8.5	1	25	0.5	4

Table S2. A comparison of the mechanical performance of DA_5-PDES-DL_2 eutectogel with the state-of-the-art hydrogel/eutectogel.

Material	Stretchability %	Tensile Fracture Strength (kPa)	Young's Modulus (kPa)	References
SP-DN	1137	23.9	——	S1
IPN	1400	~105	——	S2
PD/MnO_2	131.3	——	——	S3
Ti-PVA@PDA-Se	191.28	462.97	322.16	S4
T-ECH	610	~130	25	S5
CS hydrogel	200.05	——	0.106	S6
PPN(C4)	58	5	——	S7
AATN	1230	600	——	S8
PHA/x-CS	1430	202	13.3	S9
DA_5-PDES-DL_2	1792.54	——	220	This Work

Table S3. A comparison of the adhesion performance of DA_5-PDES-DL_2 eutectogel with the state-of-the-art hydrogel/eutectogel.

Material	Adhesion (kPa)	References
ECFGel	37.55 to collagen/tissue	S10
pdHA_t	0.78 to tissue	S11
ch-dopa-PNIPAm	1 to glass	S12
Alg/PAM/PHEA-API TN	102 to glass	S13
GelCORE	90.4 kPa to skin	S14
MC@ZIF-8/Hydrogel	10.08 to skin	S15
DA_5-PDES-DL_2	410 to glass 21 to glass (underwater)	This Work

References

S1 C. Gu, M. Wang, K. Zhang, J. Li, Y. Lu, Y. Cui, Y. Zhang and C. Liu, *Adv. Mater.*, 2022, **35**, 2208392.

S2 S. H. Shin, W. Lee, S. M. Kim, M. Lee, J. M. Koo, S. Y. Hwang, D. X. Oh and J. Park, *Chem. Eng. J.*, 2019, **371**, 452-460.

S3 S. G. Kim, J. Song, B. Ryplida, H. J. Jo, G. J. Jeong, I. Y. Kang, J. M. Patel, E. J. Jin, Y. C. Jang and S. Y. Park, *Adv. Funct. Mater.*, 2023, **3**, 2213887.

S4 M. Maitusong, T. Ren, Y. Gao, X. Hong, K. Deng, L. Yao, S. Cheng, X. Zhou, Y. Lin, G. Tian, J. Zhao, P. Li, X. Liu and J. Wang, *Adv. Funct. Mater.*, 2025, **35**, 2420683.

S5 J. Chong, C. Sung, K. S. Nam, T. Kang, H. Kim, H. Lee, H. Park, S. Park and J. Kang, *Nat. Commun.*, 2023, **14**, 2206.

S6 P. He, J. Yue, Z. Qiu, Z. Meng, J. He and D. Li, *Nat. Commun.*, 2024, **15**, 5261.

S7 D. Pranantyo, C. K. Yeo, Y. Wu, C. Fan, X. Xu, Y. S. Yip, M. I. G. Vos, S. H. Mahadevegowda, P. L. K. Lim, L. Yang, P. T. Hammond, D. I. Leavesley, N. S. Tan and M. B. Chan-Park, *Nat. Commun.*, 2024, **15**, 954.

S8 P. Song, H. Qin, H. L. Gao, H. P. Cong and S. H. Yu, *Nat. Commun.*, 2018, **9**, 2786.

S9 Y. Go, H. Y. Park, Y. Zhu, K. Yoo, J. Kwak, S. H. Jin and J. Yoon, *Adv. Funct. Mater.*, 2023, **33**, 2215193.

S10 J. Kim, H. Keum, H. Albadawi, I. Altinbasak, F. Yavuz, E. Graf, N. Mishra and R. Oklu, *Adv. Mater.*, 2025, 2503179.

S11 J. Lee, S. G. Lee, B. s. Kim, S. Park, M. N. Sundaram, B. g. Kim, C. Y. Kim and N. S. Hwang, *Adv. Sci.*, 2024, **11**, 2307353.

S12 A. Eklund, O. Ikkala and H. Zhang, *Adv. Funct. Mater.*, 2023, **34**, 2214091.

S13 S. Choi, J. R. Moon, N. Park, J. Im, Y. E. Kim, J. H. Kim and J. Kim, *Adv. Mater.*, 2022, **35**, 2206207.

S14 E. S. Sani, A. Kheirkhah, D. Rana, Z. Sun, W. Foulsham, A. Sheikhi, A. Khademhosseini, R. Dana and N. Annabi, *Sci. Adv.*, 2019, **5**, eaav1281.

S15 P. Nezhad-Mokhtari, H. Hamishehkar, M. R. Farahpour, A. Mehdipour, R. Rahbarghazi, M. Milani and M. Mehrali, *Chem. Eng. J.*, 2024, **489**, 150992.